Functional Composite Materials

RESEARCH

Open Access

Carbon composites from iron-chelating pyridine nitrogen-rich coordinated nanosheets for oxygen reduction

Bing Zhang[1], Hele Guo[1], Longsheng Zhang[2], Xu Zhang[2*], Chao Zhang[1] and Tianxi Liu[1,2*]

Abstract

The exploration of a noble-metal-free and nitrogen-doped carbon (M–N/C) composite electrocatalyst for the oxygen reduction reaction (ORR) remains a great challenge. The activities of the M–N/C composite electrocatalysts are mainly affected by the metal active sites, pyridinic nitrogen, and graphitic nitrogen. In the present work, the iron-coordinated self-assembly is proposed for the preparation of iron-chelating pyridine nitrogen-rich coordinated nanosheet (IPNCN) composites as electrocatalysts. Due to the highly conjugated structure of the IPNCN precursor, the pyridine nitrogen elements at both ends of the tetrapyrido [3,2-*a*:2′,3′-*c*:3″,2″-*h*:2‴,3‴-*j*] phenazine (TP) provide the multiple ligands, and the coordination interactions between the irons and the pyridine nitrogen further improve the thermodynamic stability, where the metal active sites and nitrogen elements are uniformly distributed in the whole structure. The resultant IPNCN composites exhibit excellent ORR performance with an onset potential of 0.93 V and a half potential of 0.84 V. Furthermore, the IPNCN composite electrocatalysts show the higher methanol resistance and electrochemical durability than the commercial Pt/C catalysts. It could be convinced that the as-designed IPNCN composite catalysts would be a promising alternative to the noble metal Pt-based catalysts in the practical applications.

Keywords: Nanosheet composites, Pyridinic nitrogen, Oxygen reduction reaction, Methanol resistance, Electrochemical durability

Introduction

The development of highly efficient electrocatalysts for energy technology has been becoming a matter of urgency as the worldwide depletion of fossil fuels and the growing demand in energy source. An enormous amount of research has been devoted for developing the non-noble oxygen reduction reaction (ORR) catalysts [1, 2]. The ORR is the crucial electrochemical process of the energy storage and the conversion devices, including the alkaline fuel cells, metal-air batteries, and proton exchange membrane fuel cells [3, 4]. The Pt-based catalysts are the most effective electrocatalysts for the ORR due to their relatively high current densities and low overpotentials [5, 6]. However, the high cost, sluggish reaction kinetics, poor methanol tolerance, and electrochemical durability have been limiting their large-scale applications in commercialization. Therefore, it is of crucial importance to explore the efficient non-noble metal catalysts with high ORR catalytic performance.

The metal-nitrogen/carbon (M–N/C, M = Fe, Co, and Ni, etc.) electrocatalysts are the most potential composite materials to replace the Pt-based catalysts since the relatively low price, the abundant reserve, the outstanding ORR catalytic performance, and the high stability [7–9]. The metal ions can serve as the catalytic centers, while the heteroatoms boost the

*Correspondence: xuzhang@jiangnan.edu.cn; txliu@jiangnan.edu.cn
[1] State Key Laboratory for Modification of Chemical Fibers and Polymer Materials, College of Materials Science and Engineering, Donghua University, Shanghai 201620, People's Republic of China
[2] Key Laboratory of Synthetic and Biological Colloids, Ministry of Education, School of Chemical and Material Engineering, International Joint Research Laboratory for Nano Energy Composites, Jiangnan University, Wuxi, Jiangsu 214122, People's Republic of China

electrocatalytic activity. The doped nitrogen can facilitate the formation of the active N–C functional sites [10, 11]. The pyridinic nitrogen (pyridinic-N) and the graphitic nitrogen (graphitic-N) are able to create the active sites which are considered to be more important factor in the ORR process [12–14]. However, the M–N/C composite catalysts generally meet several key problems, such as the structural damage and instability after carbonization, the low content of pyridinic-N and graphitic-N, and the difficulty in uniform distribution, etc. Therefore, it is necessary to design and prepare the stable M–N/C precursors from the molecular level with high content of pyridinic-N and graphitic-N to get the uniformly dispersed active sites.

In the present work, a convenient and stable self-templated method was developed to prepare the electrocatalysts of the iron-chelating pyridine nitrogen-rich coordinated nanosheet (IPNCN) composites. The IPNCN composites are capable of retaining the structural stability during carbonization since that the ligand unit of the tetrapyrido [3,2-*a*:2′,3′-*c*:3″,2″-*h*:2‴,3‴-*j*] phenazine (TP) is a fully conjugated rigid plane and is easily organized into the rigid polymers based on the coordination interactions. The TP has high nitrogen content and is rich in pyridine nitrogen from the structure design at molecular level, which can be evenly distributed in the whole skeleton of the coordination polymers. The pyridine nitrogen at both ends of the TP can form the cross-linked centers with the metal coordination interactions, while the highly conjugated structure of the TP can also create more active sites to effectively improve the electrical conductivity. In addition, the metal atoms also provide uniform and stable catalytic active sites for the ORR. Benefiting from the high content of the pyridinic-N and uniformly distributed active sites, the IPNCN composites exhibit the excellent electrocatalytic activity for the ORR and superior tolerance to methanol in comparison with the commercial Pt/C catalysts.

Experimental

Materials

The 1,10-phenanthroline-5,6-dione and ferrous chloride tetrahydrate ($FeCl_2{\cdot}4H_2O, \geq 99\%$) were purchased from Shanghai Titan Scientific Co., Ltd. The ammonium acetate (> 97.0%) and sodium hydrosulfite (> 85.0%) were purchased from TCI (Shanghai) Development Co., Ltd. The hydrochloric acid (HCl, 37%), ethanol, and methanol were purchased from the Sinopharm Chemical Regent. The deionized (DI) water was used throughout the experiments. All the purchased chemicals were used directly without further purification.

Preparation of the TP

Typically, the 1,10-phenanthroline-5,6-dione 1.45 g (6.9 mmol), sodium hydrosulfite 0.15 g (0.86 mmol), and ammonium acetate (15 g) were first placed into a dry round bottomed flask under argon, and then heated to 180 °C for 4 h with occasional stirring. After cooling to room temperature, the reaction mixtures were added into deionized water (20 ml). Then, the collected precipitations were washed with methanol and water. The obtained products were triturated in refluxing ethanol (50 ml) and filtered immediately, and then washed with ethanol and dried under vacuum. Yield: 0.92 g (63.5%). MALDI-TOF mass calculated for $C_{24}H_{12}N_6$ $[M+H]^+$, 385.11; found 384.8282. ^{1}H NMR (400 MHz, $CDCl_3$): δ (ppm) 9.67 (d, $J=7.8$ Hz, 4H), 9.37 (d, $J=2.9$ Hz, 4H), 7.87 (dd, $J=7.8$, 4.1 Hz, 4H). ^{13}C NMR (100 MHz, D_2O) δ (ppm) 151.09 (s), 144.95 (s), 137.14 (s), 129.07 (s), 122.51 (s), 119.72 (s).

Preparation of the IPNCN

The different contents (mass or mole) of TP and $FeCl_2{\cdot}4H_2O$ were added into the ethanol/water (25 ml/25 ml) mixtures. For example, the TP (61 mg, 0.16 mmol) and $FeCl_2{\cdot}4H_2O$ (32 mg, 0.16 mmol) were used to prepare the samples with $TP/Fe^{2+} \approx 1/1$. After stirring for 10 min, the mixtures were transferred into the 80 mL Teflon-lined stainless-steel autoclave and heated at 90 °C for 24 h. After being collected by filtration, washed with deionized water and ethanol, and then dried at 60 °C, the obtained products were heated-treated under the N_2 (99.99% Air Liquide) from 30 °C to 750 °C, 800 °C, 850 °C, and 900 °C with a ramp of 5 °C/min by remaining the temperature for 2 h. Next, the pyrolyzed products were cooled to room temperature and stirred in the 1 mol/L HCl for 12 h to remove the free metal particles [15]. Finally, the pyrolyzed products were collected by filtration, washed with deionized water for several times, and then dried at 60 °C. The yield of IPNCN-2–750, IPNCN-2–800, IPNCN-2–850, and IPNCN-2–900 was 55.7%, 53.9%, 51.3%, and 48.8%, respectively (Table S1).

Characterizations

The morphologies of the precursors and pyrolyzed products were characterized by the field-emission scanning electron microscopy (FESEM, JEOL S-4800). The Fourier transform infrared (FT-IR) spectra in a wavenumber range from 4000 to 600 cm^{-1} were measured by the Thermo Nicolet 6700 FT-IR Laboratory Spectrometer. The structures of the monomers were determined by the ^{1}H NMR spectrum, the ^{13}C NMR spectrum, and the MALDI-TOF mass spectrum. The ^{1}H NMR and ^{13}C NMR spectra were recorded on a Bruker model Bruker AV-400

spectrometer, operating at 400 MHz and 100 MHz, respectively. The matrix-assisted laser desorption ionization time-of-flight mass spectrometry (MALDI-TOF mass spectrum) was performed on an AB Sciex model Sciex 4800 plus MALDI-TOF analyzer, using dithranol as the matrix. The N_2 adsorption–desorption isotherms of the IPNCN composite materials were obtained by the Micromeritics ASAP-2020 at 77 K. The surface areas and pore size distributions of the tested samples were calculated by the Brunauer–Emmett–Teller (BET) and nonlocal density functional theory method. The X-ray photoelectron spectrometer measurements were conducted on a photoelectron spectrometer. The tube furnace (OTF-1200X) was used for pyrolysis of IPNCN.

Electrochemical measurements

The electrochemical measurements were carried out on a CHI 660C electrochemical workstation with a three-electrode cell (CHI600C, Shanghai, China). The working electrodes were formed by mixing the samples (5 mg) with ethanol (350 μL) and Nafion (95 μL) (5 wt%) by sonication 15 min to prepare homogeneous catalyst inks. Then, working electrode was prepared by depositing the catalyst ink onto rotating disk electrode (5 mm in diameter). The Ag/AgCl (3 mol/L) electrodes and graphite rods were employed to act as the reference and counter electrodes, respectively. All the initially tested potentials were converted to a reference hydrogen electrode (RHE) following the Eq. (1):

$$ERHE = EAg/AgCl + 0.197 + 0.059 \times pH \quad (1)$$

The cyclic voltammetry (CV) tests were performed from -0.2 to 1.2 V (*vs.* RHE) at a scan rate of 50 mV/s. The linear sweep voltammetry (LSV) was measured from 0 to 1.2 V (*vs.* RHE) at a scan rate of 5 mV/s with a rotating speed from 800 to 2400 rpm under the O_2-saturated circumstance. The current–time (i-t) tests were evaluated with 1600 rpm at 0.69 V in the O_2-saturated 0.1 mol/L KOH solution. The number of the transferred electrons (n) was calculated by the Koutecky-Levich Eqs. (2) and (3) described as follows.

$$\frac{1}{\mathrm{J}} = \frac{1}{J_K} + \frac{1}{B\omega^{1/2}} \quad (2)$$

$$n = \frac{B}{0.2F(D_0)^{2/3}(V)^{-1/6}C_{O_2}} \quad (3)$$

where the J, J_k, ω, n, F, D_0, v, and C_{O_2} is the experimentally obtained current, the mass-transport free kinetic current, the rotation rate (rpm), the number of the transferred electrons, the Faraday's constant (96,485 C/mol), the diffusion coefficient of oxygen (1.9×10^{-5} cm/s, 0.1 mol/L KOH), the kinematic viscosity of the electrolyte (0.01 cm^2/s), and the concentration of molecular oxygen in the 0.1 mol/L KOH solution (1.2×10^{-3} mol/L), respectively.

Results and discussion

The iron-chelating pyridine nitrogen-rich coordinated nanosheet (IPNCN) composites were fabricated through a convenient process, as schemed in Fig. 1a and b. The structures of the TP were determined by the MALDI-TOF mass spectrum (Fig. 1c), ^{1}H NMR spectrum (Fig. S1a), and ^{13}C NMR spectrum (Fig. S1b). A significant peak at 384.8 m/z was found in the MALDI-TOF mass spectrum (Fig. 1c), which is consistent with the molecule weight of the TP. The ^{1}H NMR spectrum (Fig. S1a) in the $CDCl_3$ (1×10^{-3} mol/L) at 25 °C displayed three highly resolved signals in the aromatic region, corresponding to the skeleton protons. In the solid-state ^{13}C NMR spectrum (Fig. S1b), the overlapping signals from 120 to 150 ppm belong to the aromatic carbons in the skeleton [16]. These results demonstrated that the novel organic ligands were successfully synthesized. The TP monomers contain up to 21.9% nitrogen element and both ends are pyridine nitrogen which can be coordinated with Fe^{2+}, so that the TP and Fe^{2+} are alternately connected to form the coordination polymers with periodic repetitive structure units. The IPNCN precursors could be easily formed because of the strong coordination interactions between the nitrogen elements and the metal ions under high temperature and high pressure [17]. The coordination polymer of IPNCN was determined by the MALDI-TOF mass spectrum. Taking the peak at 1705 m/z as an example, the polymers contain four monomers of TP and three monomers of Fe (Fig. S2). The TP and IPNCN composites were further characterized by Fourier transform infrared spectra (FT-IR) (Fig. 1d). A new absorption band at 1022 cm^{-1} for the IPNCN (TP/Fe^{2+} = 1/1) composites was observed to be assigned to the characteristic of Fe–N bonds, indicating that the coordination polymers are successfully formed [18]. Also, the literature [19] and the Gaussian calculations have showed that the main skeleton of the TP is planar. Also, the coordination form of Fe–N bonds can be further proven by Gaussian calculations. The details of the Gaussian computational method, cartesian coordinates, and electronic energies for all the complexes calculated in the present study were presented in "S3. Gaussian calculations" in the Supporting Information. In the process of coordination with Fe^{2+}, which plays a key role in connecting points, the different angles can be formed and covered between the planes, resulting in a change in thickness and length of nanosheet.

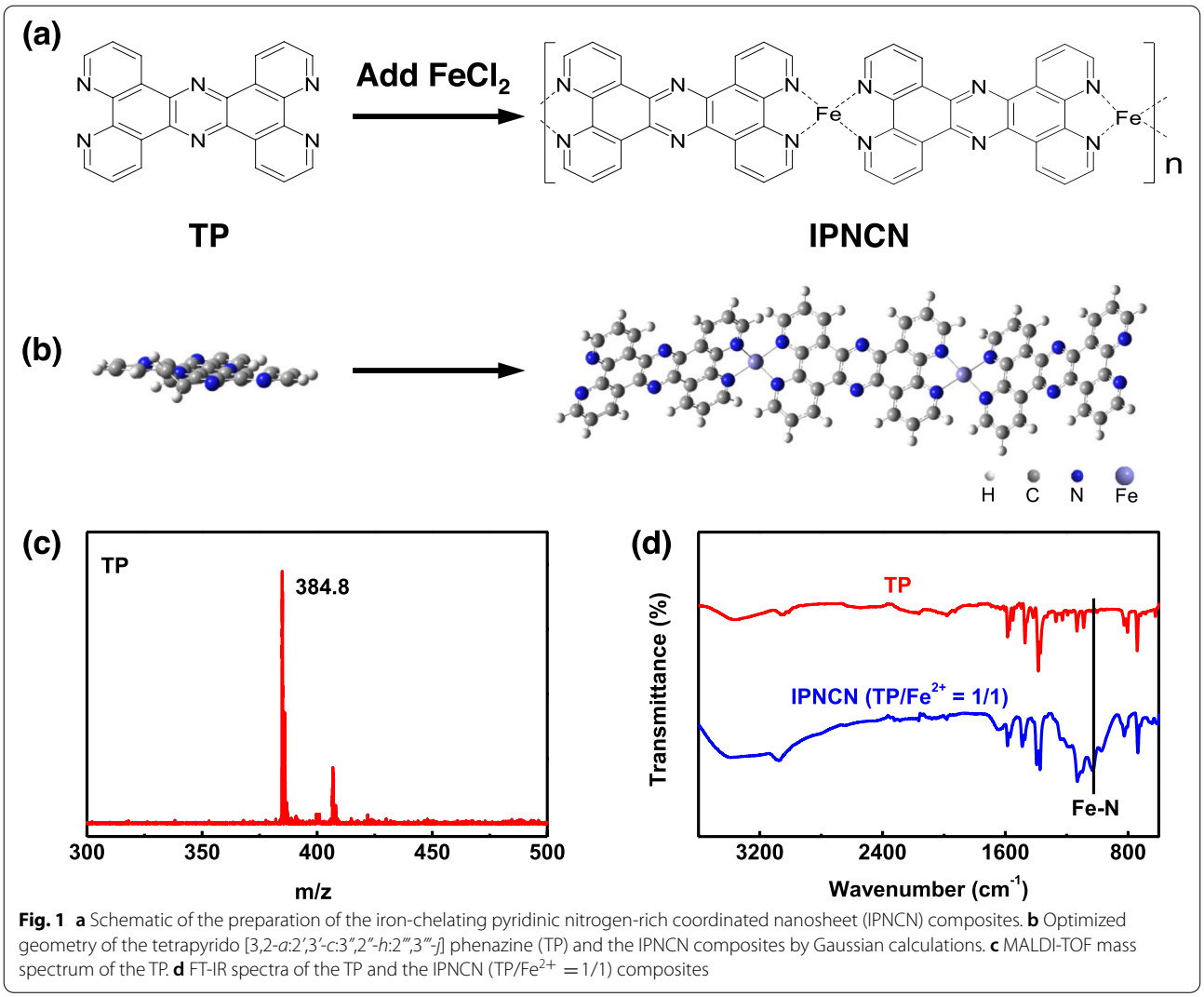

Fig. 1 **a** Schematic of the preparation of the iron-chelating pyridinic nitrogen-rich coordinated nanosheet (IPNCN) composites. **b** Optimized geometry of the tetrapyrido [3,2-*a*:2′,3′-*c*:3″,2″-*h*:2‴,3‴-*j*] phenazine (TP) and the IPNCN composites by Gaussian calculations. **c** MALDI-TOF mass spectrum of the TP. **d** FT-IR spectra of the TP and the IPNCN (TP/Fe^{2+} = 1/1) composites

To obtain the coordination polymers with different degree of reaction, the different mole ratios of TP to Fe^{2+} were adjusted among TP/Fe^{2+} = 2/1, TP/Fe^{2+} = 1/1, and TP/Fe^{2+} = 1/2, named as IPNCN-1, IPNCN-2, and IPNCN-3, respectively. The IPNCN samples burning at different calcinate temperatures were denoted as IPNCN-1–850, IPNCN-2-X (X = 750, 800, 850, and 900), and IPNCN-3–850, where the last character of X stands for the calcinate temperature. The TP-850 represents the TP samples which do not coordinate with metals and are calcined at 850 oC. Notably, the TP can also form the planar sheets due to the strong intermolecular large conjugated aromatic structures. The microstructures of the TP were characterized by the emission scanning electron microscopy (SEM) which shows the scale-like nanosheets (Fig. 2a), indicating the consistency of the microstructures and the chemical structures. After coordinating with the metal ions through solvothermal method under high temperature and high pressure, the nanosheets still remain but the size was changed (Fig. 2c) [20]. The reason is that the metal ions in the center can connect the planar flake structures and the both ends of the pyridine nitrogen from TP can coordinate with central metal ions at different angles in the three-dimensional space, resulting in the angle changes between the nanosheets [21]. The nanosheet morphologies of the TP were changed after calcination at 850 °C in the nitrogen atmosphere, and the flake morphologies would shrink and accumulate (Fig. 2b). However, the sheets of the IPNCN-2–750, IPNCN-2–800, IPNCN-2–850, IPNCN-2–900, IPNCN-1–850, and IPNCN-3–850 are still existed (Fig. 2d, e, f, and S3), reflecting that the coordination interactions are beneficial to improving the thermal stability of the large conjugated aromatic structures.

The stability at different calcination temperatures was mainly benefited from the fully conjugated rigid planes

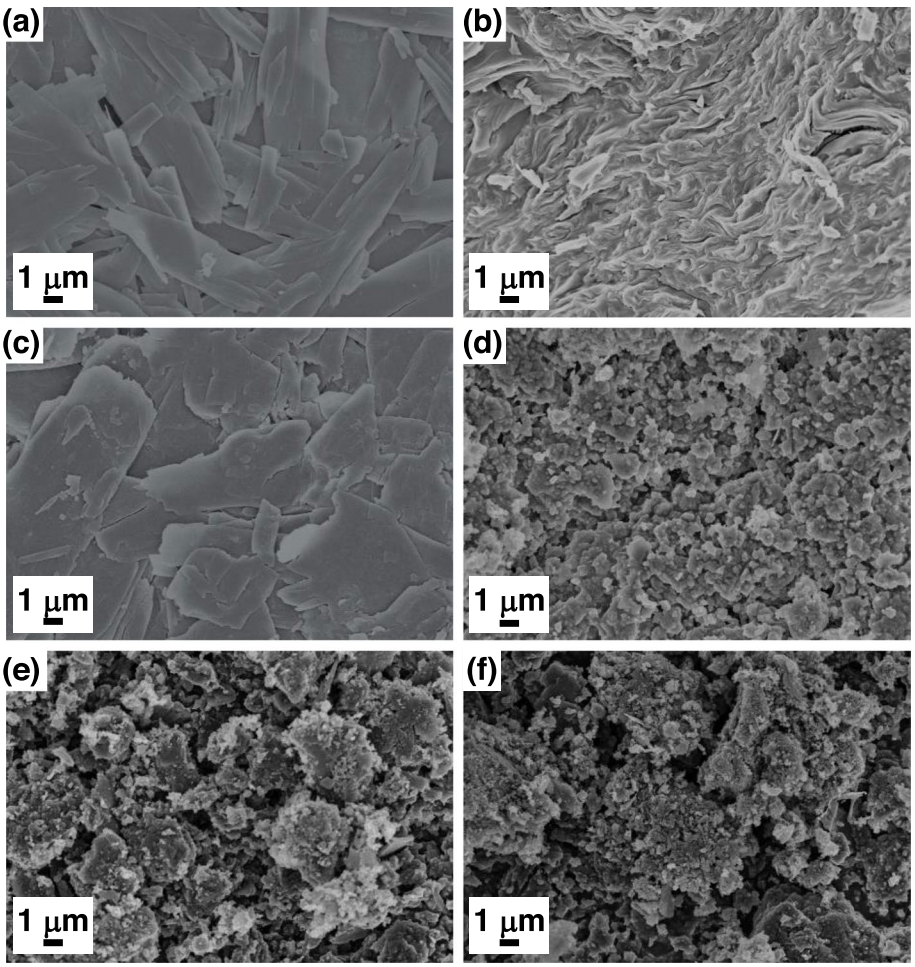

Fig. 2 SEM image of the **a** TP, **b** TP-850, **c** IPNCN-2 composites, **d** IPNCN-2–800 composites, **e** IPNCN-2–850 composites, and **f** IPNCN-2–900 composites

of the TP and the rigid polymers of the IPNCN-2 composites. The planar structures of the TP are also capable of acting as the templates for metals, which is favorable to coordination with metals and full contact with oxygen during the oxygen reduction reaction process [22]. The advantage of such design is the homogeneous distribution of the nitrogen and the uniformly dispersed metal catalytic active sites [23], which prevents the agglomeration of the metals in the calcination process. Therefore, it can be convinced from the above-mentioned results and discussion that the self-stable carbonization strategy has been discovered, which would provide a reference for the selection of the stable catalytic materials.

To examine the chemical constitutions of the as-prepared IPNCN composites, the X-ray photoelectron spectroscopy (XPS) measurements were further performed, as presented in Fig. 3 and Figure S4 and S5 in the Supporting Information. The existence of the C, N, O, and Fe elements in the IPNCN-2–850 can be convinced from Fig. 3a, corresponding to the spectra peaks around 285, 399, 531, and 715 eV, respectively. The chemical elements of the IPNCN-2-X composites were counted and summarized in Table 1, indicating that the nitrogen atoms have been successfully doped into the IPNCN-2-X composites. The high-resolution C 1 s spectra displayed four peaks at 284.58, 285.15, 286.12, and 288.56 eV (Fig. 3b), assigning to the C–C, C-N, C-O, and C=O groups, respectively [24]. The N 1 s peaks can be divided into 398.23, 400.24, 401.00, and 402.73 eV (Fig. 3c), corresponding to the pyridinic-N, pyrrolic-N, graphitic-N, and N-oxide (N–O), respectively [25]. The contents of the different nitrogen species were also calculated and listed in Table 1. It can be seen that pyridinic-N and graphitic-N still have relatively high contents at high temperature, and the pyridinic-N and graphitic-N can serve as the efficient active sites during the oxygen reduction reaction process [26]. The total nitrogen content decreases from 11.14 at. % to 3.24 at. % with the increase of pyrolysis temperature

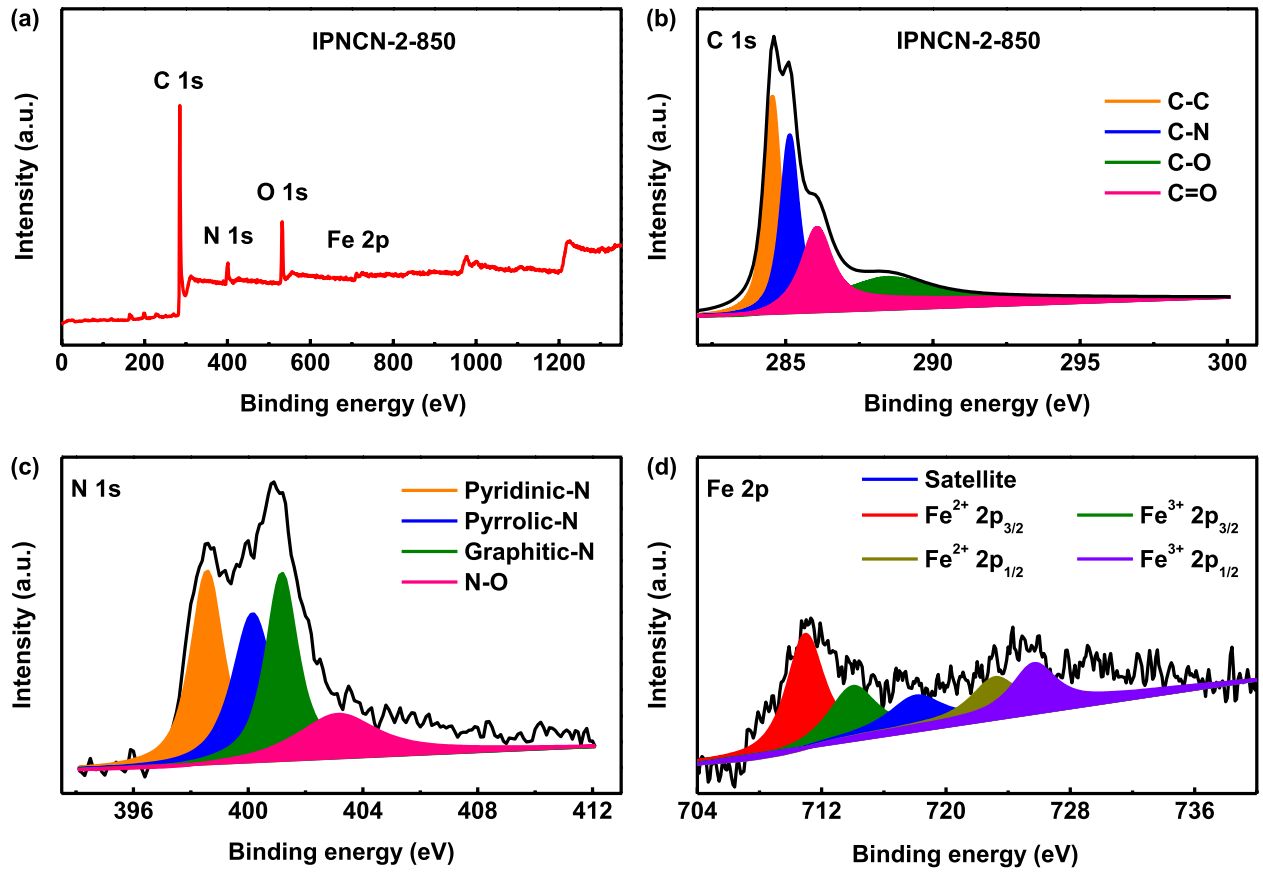

Fig. 3 **a** XPS survey spectra of the IPNCN-2–850 composites. The high-resolution **b** C 1 s, **c** N 1 s, and **d** Fe 2p XPS spectra of the IPNCN-2–850 composites

Table 1 Summary of the nitrogen content and bonding state of the IPNCN-2-X composite catalysts

Sample	C (at. %)	N (at. %)	O (at. %)	Fe (at. %)	XPS (N content %)			Pyridinic-N (at. %)
					Pyridinic-N	Pyrrolic-N	Graphitic-N	
IPNCN-2–750	77.5	11.1	10.0	1.4	34.3	29.4	26.9	3.8
IPNCN-2–800	79.0	9.21	10.8	1.0	33.7	27.9	25.2	3.1
IPNCN-2–850	79.5	8.3	10.9	1.2	29.3	27.8	27.7	2.4
IPNCN-2–900	84.5	3.2	11.4	0.9	30.1	30.5	28.1	1.0

from 750 to 900 °C due to the decomposition of the N–C bonds at high temperature [27, 28]. However, the proportion of the pyridinic-N (27.8% in Table 1) in the IPNCN-2–850 composites could still strongly support the outstanding oxygen reduction reaction activity. The high-resolution Fe 2p XPS spectra of the IPNCN-2–850 composites in Fig. 3d are divided into individual peaks. The binding energy peak at 710.97, 714.08, 718.16, 723.30, and 725.76 eV corresponds to the $2p_{3/2}$ orbit of Fe^{2+}, the $2p_{3/2}$ orbit of Fe^{3+}, the satellite peak, the $2p_{1/2}$ orbit of Fe^{2+}, and the $2p_{1/2}$ orbit of Fe^{3+}, respectively. The Fe^{2+} groups act as the role of the active sites, promoting the adsorption of O_2 and boosting the catalytic activity of the IPNCN composites [26, 29, 30]. The XRD spectra of IPNCN-2 after pyrolysis were also presented in Fig. S6. The peak around 25° becomes narrower and stronger during the increasing temperature, indicating that more ordered graphitic carbon was produced at a higher pyrolysis temperature [31]. The content of iron in the different composites were further detected by Inductively Coupled

Plasma (ICP). With the increase of pyrolysis temperature, the content of iron decreases gradually (Table S2).

The surface areas and pore structures of the IPNCN-2 composite catalysts were determined by the nitrogen isothermal adsorption–desorption measurements through the Brunauer–Emmett–Teller (BET) (Fig. 4). The IPNCN-2-X composite catalysts exhibit an obvious of type-IV isotherm characteristics with H1 hysteresis loop (Fig. 4a) [32, 33], which is the characteristic of the disordered micro-/meso-porous materials. The details of the BET surface areas and pore size distributions of the IPNCN-2 composite catalysts were listed in Table 2. The BET surface area of the IPNCN-2–750, IPNCN-2–800, IPNCN-2–850, and IPNCN-2–900 composite catalysts is 13.0, 14.1, 12.0, and 34.2 $m^2\ g^{-1}$, respectively. The decrease of the surface area for the IPNCN-2–850 is mainly due to the changing of the pores, while the increase of the surface area for the IPNCN-2–900 ascribes to the decomposition of the small organic molecules at relatively high temperature [34]. The IPNCN-2-X composite catalysts have the mesopores with large sizes and the nanopores

Table 2 The BET surface areas and pore size distributions of the IPNCN-2 composite catalysts

Sample	S_{BET} ($m^2\ g^{-1}$)	Pore volume (mL g^{-1})		
		Total	Micro	Meso
IPNCN-2–750	13.000	0.030	0.011	0.021
IPNCN-2–800	14.100	0.040	0.013	0.029
IPNCN-2–850	12.000	0.040	0.005	0.037
IPNCN-2–900	34.223	0.091	0.026	0.064

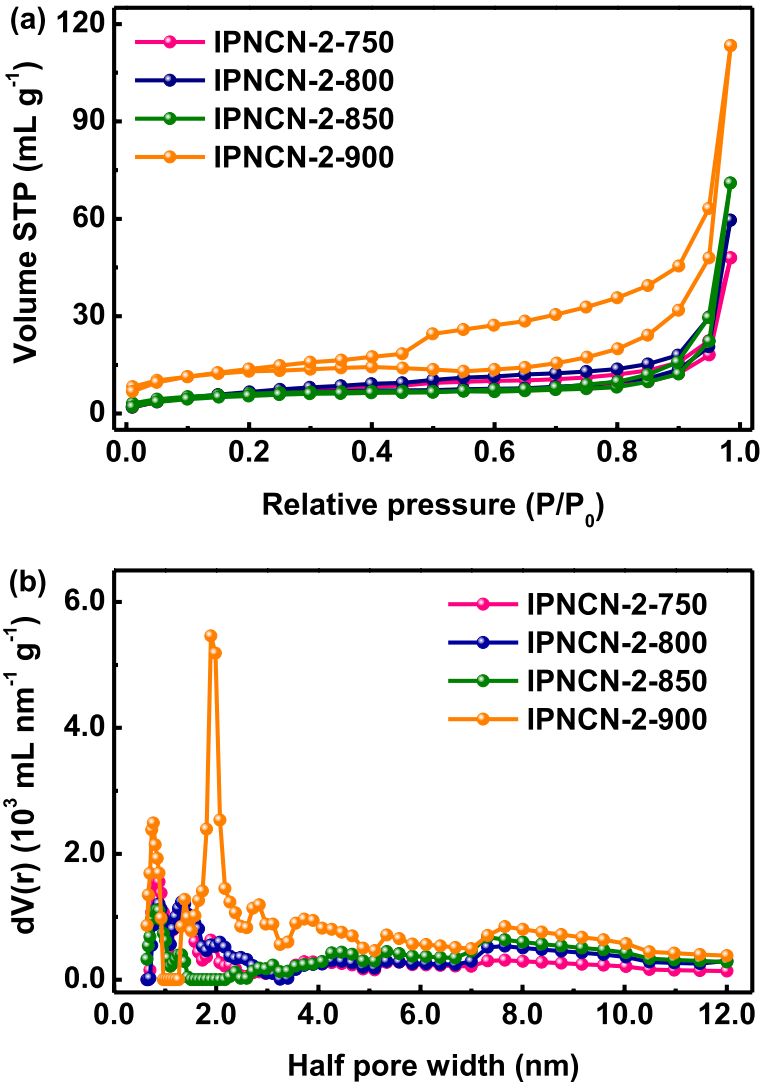

Fig. 4 **e** Nitrogen sorption/desorption isotherms and **f** half pore-size distributions of the IPNCN-2 composite catalysts prepared at different pyrolytic temperatures

with small sizes that can be beneficial for the catalysis process and provide the more abundant active sites, respectively [35].

To explore the ORR catalytic performances, the cyclic voltammetry (CV) measurements in the N_2-saturated and O_2-saturated 0.1 mol/L potassium hydroxide (KOH) solution for the IPNCN-2–850 composite catalysts were further performed on a rotating disk electrode (RDE) at the scan rate of 50 mV s^{-1} (Fig. 5). Fig. 5a depicts that the redox peak could not be found in the N_2-saturated electrolyte, while a well-defined cathodic reduction peak at 0.80 V was clearly observed in the O_2-saturated KOH electrolyte, suggesting an obvious intrinsic electrocatalytic activity for the ORR [36, 37]. For comparison, the apparent peak at 0.76, 0.78, and 0.80 V was observed for the IPNCN-2–750, IPNCN-2–800, and IPNCN-2–900 composite catalysts in the O_2-saturated electrolyte, respectively (Fig. S7a). The cathodic reduction current peak at about 0.81 V (*vs.* RHE) of the IPNCN-2–850 composite catalysts was higher than that of other samples (Fig. 5a, Fig. S7a, and Fig. S7b), indicating that the IPNCN-2–850 composite catalysts have the best ORR activity among others. To further explore the electrocatalytic properties of the IPNCN-2-X composite catalysts, the linear sweep voltammogram (LSV) measurements were carried out by using the rotating disk electrode (RDE) in the O_2-saturated 0.1 mol/L KOH solution (Fig. 5b). The IPNCN-2–850 composite catalysts showed excellent onset potentials of 0.93 V and half-wave potentials of 0.84 V (*vs.* RHE), which can

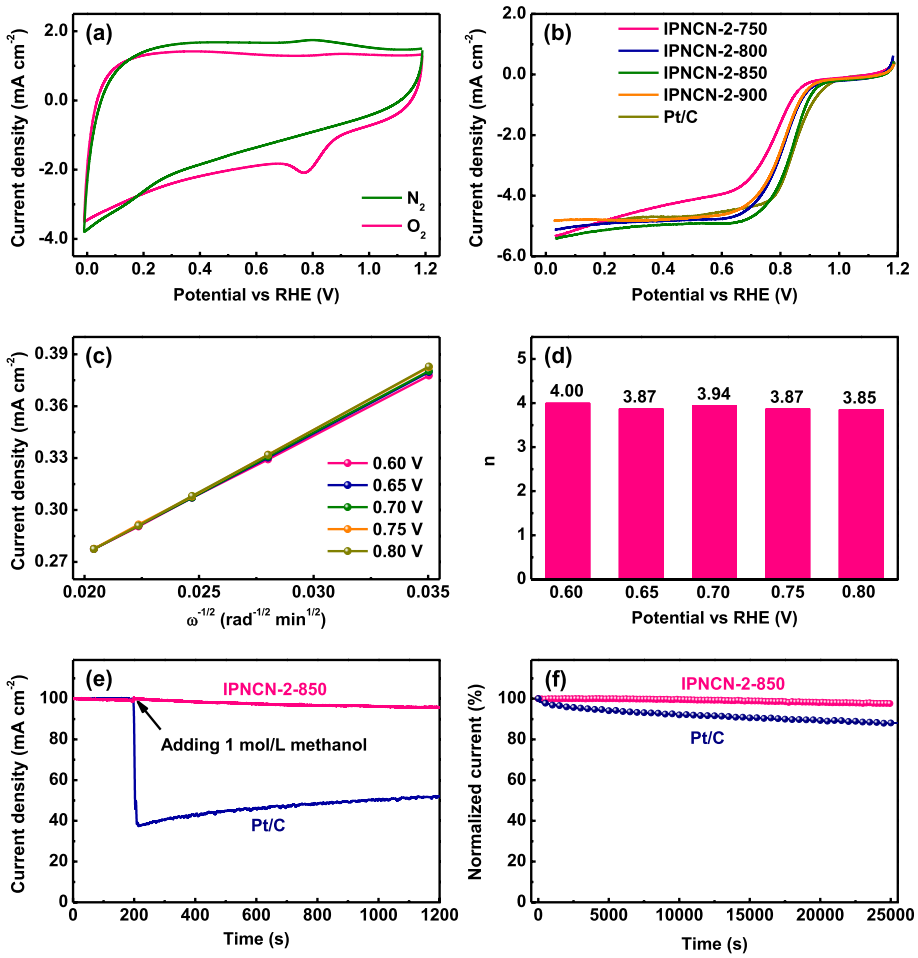

Fig. 5 **a** CV curves of the IPNCN-2–850 composite catalysts in the N_2-saturated and O_2-saturated 0.1 mol/L aqueous KOH solutions. **b** LSV curves of the IPNCN-2 composite catalysts prepared at different pyrolytic temperatures and the commercial Pt/C catalysts at 1600 rpm rotation rate in the O_2-saturated 0.1 mol/L KOH solution. **c** K-L plots for the IPNCN-2–850 composite catalysts at different electrode potentials from 0.60 to 0.80 V (vs RHE). **d** Calculated electron transfer number of the IPNCN-2–850 composite catalysts. **e** Methanol tolerance evaluation of the IPNCN-2–850 composite and Pt/C catalysts. **f** Current–time **i**-**t** test of the IPNCN-2–850 composite catalysts at 1600 rpm rotation rate in the O_2-saturated 0.1 mol/L KOH solution

compare to the commercial Pt/C catalysts with onset potentials of 0.96 V and half-wave potentials of 0.85 V (*vs.* RHE). Among the IPNCN catalysts, the ORR activity of the IPNCN-2–850 composite catalysts are better than those of IPNCN-2–750, IPNCN-2–900, IPNCN-1–850, and IPNCN-3–850 (Fig. 5b and Fig. S7c), implying an excellent ORR performance for the stable IPNCN composite catalysts [38]. Furthermore, the limiting current density of the IPNCN-2–850 composite catalysts is also better than that of the Pt/C catalysts. Therefore, the IPNCN-2–850 composite was used for further exploration. The high ORR performance was ascribed to high metal utilization efficiency and fast mass transport [39, 40]. In addition, the planar structures could further provide sufficient contact points for oxygen to promote the ORR catalytic performance [41].

The linear sweep voltammetry (LSV) curves of the IPNCN-2–850 composite catalysts varying from 400 to 2400 rpm in the O_2-saturated 0.1 mol/L KOH solution were further presented in Fig. S7d. The limiting current density obtained from the LSV curves shows a rapid increase as the rotation speed increases, which is due to the decrease of the diffusion distance under high-speed condition. The corresponding Koutecky-Levich (K-L) plots of the IPNCN-2–850 composite catalysts at different potentials exhibit a great linearity and some are overlapped (Fig. 5c), indicating a similar electron-transfer process. The electron transfer number (n) of the IPNCN-2–850 composite catalysts was calculated as 3.9 in average at various potentials from 0.2 to 0.6 V according the K-L plot (Fig. 5d), indicating that the oxygen is reduced through a direct four-electron pathway.

For comparison, the TP catalysts were prepared via the same method for preparing the IPNCN-2–850 composite catalysts but without the addition of ferrous chloride, which were named as TP-850. The ORR activities of the TP-850 catalysts were observed as not good as the IPNCN-2–850 composite catalysts (Fig. S7e and Fig. S7f), suggesting the importance of the iron ions which are able to form the active sites. In order to prove the importance of the coordination interactions in the solvothermal process, the direct method of grinding TP and ferrous chloride was employed instead of the solvothermal method to prepare the Grind-TP-Fe-2–850 catalysts. The Grind-TP-Fe-2–850 catalysts also show the much lower onset potential and half-wave potential than the IPNCN-2–850 composite catalysts (Fig. S7e and Fig. S7f), indicating that the solvothermal method is conducive to form the coordination polymers and the uniform dispersion of the active sites [42–44]. The catalytic mechanism of IPNCN after high pyrolysis temperatures for efficient ORR could be attributed to the high content of the pyridinic-N and uniformly distributed active sites (Fig. 6). The pyridinic-N functionality is active for facilitating ORR at a low overpotential via the 4-electron pathway [45].

In addition to the ORR activity, the electrochemical stability is another important aspect for the ORR catalysts in the practical applications. The methanol resistance and electrochemical durability of the IPNCN-2–850 composite and Pt/C catalysts were characterized by the chronoamperometry measurements. After injecting the solution of methanol (1 mol/L), the Pt/C catalysts show an immediate drop in the current density. However, there is no obvious change in the current density for the IPNCN-2–850 composite catalysts during the ORR

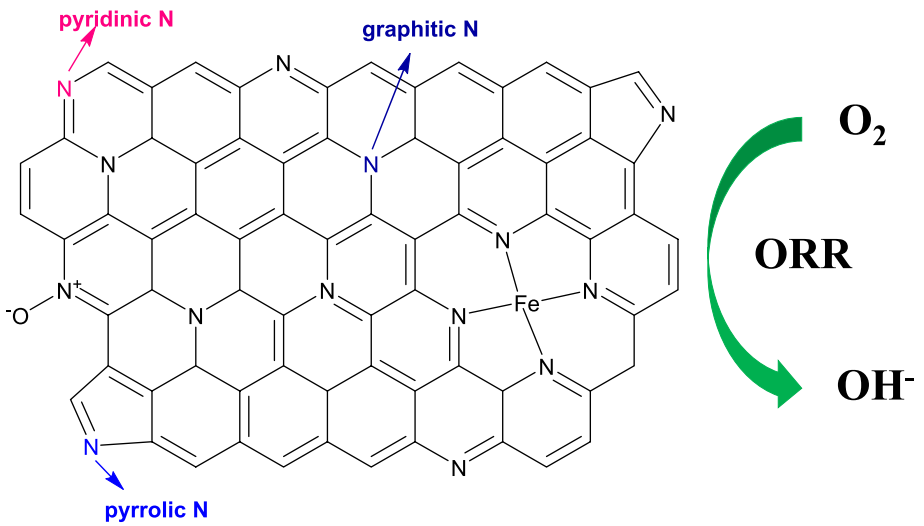

Fig. 6 The mechanism of the IPNCN after pyrolysis for ORR

process (Fig. 5e), revealing that the IPNCN-2–850 composite catalysts have the great tolerance to the methanol. Moreover, another significant parameter to detect the catalytic performance is the electrochemical durability, as illustrated in Fig. 5f. The IPNCN-2–850 composite catalysts still keep 97.7% of the initial current while the Pt/C catalysts retain only 69% of the initial current after 40,000 s (Fig. 5f). Furthermore, a small negative half-potential shift was observed after the stability test (Fig. S8), further demonstrating the reliable stability of IPNCN-2–850 as ORR electrocatalysts. It could be concluded that the as-prepared IPNCN-2–850 composite catalysts possess the much better methanol tolerance and electrochemical durability [46].

Conclusions

In summary, the novel planar organic ligands (IPNCN composites) were successfully designed and synthesized, where the large content of pyridine nitrogen and full conjugated systems are beneficial to improving the structural stability. The IPNCN composites can be served as the templates for metal ions through the solvothermal method to obtain the more stable catalyst precursors. The design strategy of IPNCN composite catalysts is conducive to self-stabilization in high temperature environment. The results revealed that the as-prepared IPNCN composite catalysts possess the more excellent ORR catalytic performance in the alkaline solutions compared to the commercial Pt/C catalysts. The superior catalytic activity of the IPNCN composite catalysts can be attributed to the rich content of pyridine nitrogen, the stable and uniform distribution of the nitrogen elements and the metal catalyzed active sites. The methanol resistance and electrochemical durability of the IPNCN composite catalysts are much better than those of the commercial Pt/C catalysts in the alkaline media. It could be convinced that the as-designed IPNCN composite catalysts would be a promising alternative to the noble metal Pt-based catalysts in the practical applications.

Abbreviations

ORR: Oxygen reduction reaction; IPNCN: Iron-chelating pyridine nitrogen-rich coordinated nanosheet; TP: Tetrapyrido [3,2-*a*:2′,3′-*c*:3″,2″-*h*:2‴,3‴-*j*] phenazine; M–N/C: Metal-nitrogen/carbon; RHE: Reference hydrogen electrode; XPS: X-ray photoelectron spectroscopy; DI water: Deionized water; FESEM: Field-emission scanning electron microscopy; BET: Brunauer–Emmett–Teller; CV: Cyclic voltammetry (CV); LSV: Linear sweep voltammetry; RDE: Rotating disk electrode; K-L: Koutecky-Levich; i-t: Current–time; n: Number of the transferred electrons; J: Experimentally obtained current; J_k: Mass-transport free kinetic current; ω: Rotation rate (rpm); F: Faraday's constant (96,485 C/mol); D_0: Diffusion coefficient of oxygen (1.9×10^{-5} cm/s, 0.1 mol/L KOH); v: Kinematic viscosity of the electrolyte (0.01 cm^2/s); c_{O_2} : Concentration of molecular oxygen in the 0.1 mol/L KOH solution (1.2×10^{-3} mol/L.

Supplementary Information

The online version contains supplementary material available at https://doi.org/10.1186/s42252-022-00030-y.

Additional file 1.

Acknowledgements

Supports from the National Natural Science Foundation of China (52122303, 21875033, 52103074), the Natural Science Foundation of Shanghai (21ZR1402800), and the China Postdoctoral Science Foundation (2021M690597) are appreciated.

Authors' contributions

BZ carried out the whole study and drafted the manuscript. HG participated the preparations and characterizations. LZ participated the characterizations, helped to draft the manuscript. XZ analyzed the results of characterizations, reviewed the manuscript, and provided the funding supports. CZ conceived of the study, concluded the results, reviewed the manuscript, and provided the funding supports. TL leaded the whole study, helped to conceive of the study, and provided the funding supports. All the authors have read and approved the final manuscript.

Funding

This work was financially supported by the National Natural Science Foundation of China (52122303, 21875033, 52103074), the Natural Science Foundation of Shanghai (21ZR1402800), and the China Postdoctoral Science Foundation (2021M690597).

Availability of data and materials

All data generated or analyzed during this study are included in this published article and its supplementary information files.

Declarations

Ethics approval and consent to participate

Not applicable.

Competing interests

The authors declare that they have no competing interests.

Consent for publication

Not applicable.

Received: 30 November 2021 Accepted: 4 March 2022
Published online: 14 March 2022

References

1. C. Su, Y. Liu, Z. Luo, J.-P. Veder, Y. Zhong, S.P. Jiang, Z. Shao, Defects-rich porous carbon microspheres as green electrocatalysts for efficient and stable oxygen-reduction reaction over a wide range of pH values. Chemical Engineering Journal 406, 126883 (2021)
2. J. Tang, C. Su, Y. Zhong, Z. Shao, Oxide-based precious metal-free electrocatalysts for anion exchange membrance fuel cells: from material design to cell applications. Journal of Materials Chemistry A 9, 3151–3179 (2021)
3. J. Han, J. Bian, C. Sun, Recent advances in single-atom electrocatalysts for oxygen reduction reaction. Research 2020, 9512763 (2020)
4. G.J. He, Y.Y. Liu, D.E. Gray, J. Othon, Conductive polymer composites cathodes for rechargeable aqueous Zn-ion batteries A mini-review. Composites Communications 27, 100882 (2021)
5. C. Cui, L. Gan, M. Heggen, S. Rudi, P. Strasser, Compositional segregation in shaped Pt alloy nanoparticles and their structural behaviour during electrocatalysis. Nat. Mater. 12, 765–771 (2013)
6. D. Zhao, Z. Zhuang, X. Cao, C. Zhang, Q. Peng, C. Chen, Y. Li, Atomic site electrocatalysts for water splitting, oxygen reduction and selective oxidation. Chem. Soc. Rev. 49, 2215–2264 (2020)

7. Y. Chen, S. Ji, Y. Wang, J. Dong, W. Chen, Z. Li, R. Shen, L. Zheng, Z. Zhuang, D. Wang, Y. Li, Isolated single iron atoms anchored on N-doped porous carbon as an efficient electrocatalyst for the oxygen reduction reaction. Angew. Chem. Int. Ed. 56, 6937–6941 (2017)
8. Z.P. Wang, L. Chen, S.D. Xu, D. Zhang, X.X. Zhou, X. Wu, X.M. Xie, X.Y. Qiu, Cobalt vanadium layered double hydroxide/FeOOH heterostructure catalyst with strong electron interactions for stable oxygen evolution performance. Composites Communications 27, 100780 (2021)
9. L. Wu, L. Yu, X. Xiao, F. Zhang, S. Song, S. Chen, Z. Ren, Recent advances in self-supported layered double hydroxides for oxygen evolution reaction. Research 2020, 3976278 (2020)
10. G. Wu, K.L. More, C.M. Johnston, P. Zelenay, High-performance electrocatalysts for oxygen reduction derived from polyaniline, iron, and cobalt. Science 332, 443–447 (2011)
11. K. Gong, F. Du, Z. Xia, M. Durstock, L. Dai, Nitrogen-doped carbon nanotube arrays with high electrocatalytic activity for oxygen reduction. Science 323, 760–764 (2009)
12. Y. Nie, L. Li, Z. Wei, Recent advancements in Pt and Pt-free catalysts for oxygen reduction reaction. Chem. Soc. Rev. 44, 2168–2201 (2015)
13. D. Guo, R. Shibuya, C. Akiba, S. Saji, T. Kondo, J. Nakamura, Active sites of nitrogen-doped carbon materials for oxygen reduction reaction clarified using model catalysts. Science 351, 361–365 (2016)
14. X.Y. Cui, S.B. Yang, X.X. Yan, J.G. Leng, S. Shuang, P.M. Ajayan, Z.J. Zhang, Pyridinic-nitrogen-dominated graphene aerogels with Fe-N-C coordination for highly efficient oxygen reduction reaction. Adv. Func. Mater. 26, 5708–5717 (2016)
15. Q. Lai, L. Zheng, Y. Liang, J. He, J. Zhao, J. Chen, Metal-organic-framework-derived Fe-N/C electrocatalyst with five-coordinated Fe-N_x sites for advanced oxygen reduction in acid media. ACS Catal. 7, 1655–1663 (2017)
16. B. Zhang, X. Zhang, K. Wan, J. Zhu, J. Xu, C. Zhang, T. Liu, Dense hydrogen-bonding network boosts ionic conductive hydrogels with extremely high toughness, rapid self-recovery, and autonomous adhesion for human-motion detection. Research 2021, 9761625 (2021)
17. C. Tang, Q. Zhang, Nanocarbon for oxygen reduction electrocatalysis Dopants, edges, and defects. Advanced Materials 29, 160413 (2017)
18. M. Jahan, Q. Bao, K.P. Loh, Electrocatalytically active graphene-porphyrin MOF composite for oxygen reduction reaction. J. Am. Chem. Soc. 134, 6707–6713 (2012)
19. Y.F. Song, P. Yang, Mononuclear tetrapyrido [3,2-a : 2′,3′-c : 3",2"-h : 2'",3"'-j] phenazine (tpphz) cobalt complex. Polyhedron 20, 501–506 (2001)
20. Y. Mun, M.J. Kim, S.A. Park, E. Lee, Y. Ye, S. Lee, Y.T. Kim, S. Kim, O.H. Kim, Y.H. Cho, Y.E. Sung, J. Lee, Soft-template synthesis of mesoporous non-precious metal catalyst with Fe-N_x/C active sites for oxygen reduction reaction in fuel cells. Applied Catalysis B-Environmental 222, 191–199 (2018)
21. S. Liu, Z. Wang, S. Zhou, F. Yu, M. Yu, C.Y. Chiang, W. Zhou, J. Zhao, J. Qiu, Metal-organic-framework-derived hybrid carbon nanocages as a bifunctional electrocatalyst for oxygen reduction and evolution. Adv. Mater. 29, 1700874 (2017)
22. J. Wang, S. Kattel, Z. Wang, J.G. Chen, C.J. Liu, L-phenylalanine-templated platinum catalyst with enhanced performance for oxygen reduction reaction. ACS Appl. Mater. Interfaces. 10, 21321–21327 (2018)
23. H.W. Liang, W. Wei, Z.S. Wu, X. Feng, K. Mullen, Mesoporous metal-nitrogen-doped carbon electrocatalysts for highly efficient oxygen reduction reaction. J. Am. Chem. Soc. 135, 16002–16005 (2013)
24. W.J. Jiang, L. Gu, L. Li, Y. Zhang, X. Zhang, L.J. Zhang, J.Q. Wang, J.S. Hu, Z. Wei, L.J. Wan, Understanding the high activity of Fe-N-C electrocatalysts in oxygen reduction: Fe/Fe_3C nanoparticles boost the activity of Fe-N_x. J. Am. Chem. Soc. 138, 3570–3578 (2016)
25. J. Guo, Y. Li, Y. Cheng, L. Dai, Z. Xiang, Highly efficient oxygen reduction reaction electrocatalysts synthesized under nanospace confinement of metal-organic framework. ACS Nano 11, 8379–8386 (2017)
26. Y. Zhu, B. Zhang, X. Liu, D.W. Wang, D.S. Su, Unravelling the structure of electrocatalytically active Fe-N complexes in carbon for the oxygen reduction reaction. Angew. Chem. Int. Ed. 53, 10673–10677 (2014)
27. J. Hu, L.J. Cao, Z.Y. Wang, J.L. Liu, J.N. Zhang, Y.L. Cao, Z.G. Lu, H. Cheng, Hollow high-entropy metal organic framework derived nanocomposite as efficient electrocatalyst for oxygen reduction reaction. Composites Communications 27, 100866 (2021)
28. K. Chen, K. Liu, P. An, H. Li, Y. Lin, J. Hu, C. Jia, J. Fu, H. Li, H. Liu, Z. Lin, W. Li, J. Li, Y.R. Lu, T.S. Chan, N. Zhang, M. Liu, Iron phthalocyanine with coordination induced electronic localization to boost oxygen reduction reaction. Nat. Commun. 11, 4173 (2020)
29. F.L. Meng, Z.L. Wang, H.X. Zhong, J. Wang, J.M. Yan, X.B. Zhang, Reactive multifunctional template-induced preparation of Fe-N-doped mesoporous carbon microspheres towards highly efficient electrocatalysts for oxygen reduction. Adv. Mater. 28, 7948–7955 (2016)
30. G. Yang, J. Zhu, P. Yuan, Y. Hu, G. Qu, B.A. Lu, X. Xue, H. Yin, W. Cheng, J. Cheng, W. Xu, J. Li, J. Hu, S. Mu, J.N. Zhang, Regulating Fe-spin state by atomically dispersed Mn-N in Fe-N-C catalysts with high oxygen reduction activity. Nat. Commun. 12, 1734 (2021)
31. L. Lin, Q. Zhu, A.-W. Xu, Noble-metal-free Fe-N-C catalyst for highly efficient oxygen reduction reaction under both alkaline and acidic conditions. J. Am. Chem. Soc. 136, 11027–11033 (2014)
32. Y. Zheng, S. Chen, K.A.I. Zhang, J. Zhu, J. Xu, C. Zhang, T. Liu, Ultrasound-triggered assembly of covalent triazine framework for synthesizing heteroatom-doped carbon nanoflowers boosting metal-free bifunctional electrocatalysis. ACS Appl. Mater. Interfaces. 13, 13328–13337 (2021)
33. X. Tang, Y. Wu, W. Zhai, T. Chu, L. Li, B. Huang, T. Hu, K. Yuan, Y. Chen, Iron-based nanocomposites implanting in N, P Co-doped carbon nanosheets as efficient oxygen reduction electrocatalysts for Zn-Air batteries. Composites Communications 29, 100994 (2021)
34. S. Chen, Y. Zheng, B. Zhang, Y. Feng, J. Zhu, J. Xu, C. Zhang, W. Feng, T. Liu, Cobalt, nitrogen-doped porous carbon nanosheet-assembled flowers from metal-coordinated covalent organic polymers for efficient oxygen reduction. ACS Appl. Mater. Interfaces. 11, 1384–1393 (2019)
35. S. Serov, K. Artyushkova, P. Atanassov, Fe-N-C oxygen reduction fuel cell catalyst derived from carbendazim: Synthesis, structure, and reactivity. Adv. Energy Mater. 4, 1301735 (2014)
36. J. Shui, M. Wang, F. Du, L. Dai, N-doped carbon nanomaterials are durable catalysts for oxygen reduction reaction in acidic fuel cells. Science Advances 1, e1400129 (2015)
37. X. Zhang, W. Fan, T.X. Liu, Fused deposition modeling 3D printing of polyamide-based composites and its applications. Composites Communications 21, 100413 (2020)
38. H.J. Shen, E. Gracia-Espino, J.Y. Ma, H.D. Tang, X. Mamat, T. Wagberg, G.Z. Hu, S.J. Guo, Atomically FeN_2 moieties dispersed on mesoporous carbon: A new atomic catalyst for efficient oxygen reduction catalysis. Nano Energy 35, 9–16 (2017)
39. R. Jiang, L. Li, T. Sheng, G. Hu, Y. Chen, L. Wang, Edge-Site engineering of atomically disepersed Fe-N_4 by selective C-N bond cleavage for enhanced oxygen eduction reaction activities. J. Am. Chem. Soc. 140, 11594–11598 (2018)
40. T. Marshall-Roth, N.J. Libretto, A.T. Wrobel, K.J. Anderton, M.L. Pegis, N.D. Ricke, T.V. Voorhis, J.T. Miller, Y. Surendranath, Apyridinic Fe-N_4 macrocycle models the active sites in Fe/N-doped carbon electrocatalysts. Nature Commmunications 11, 5283 (2020)
41. W.P. van den Wildenberg, G.J. van Boxtel, M.W. van der Molen, D.A. Bosch, J.D. Speelman, C.H. Brunia, Stimulation of the subthalamic region facilitates the selection and inhibition of motor responses in Parkinson's disease. J. Cogn. Neurosci. 18, 626–636 (2006)
42. C. Zhang, Y.C. Wang, B. An, R. Huang, C. Wang, Z. Zhou, W. Lin, Networking pyrolyzed zeolitic imidazolate frameworks by carbon nanotubes improves conductivity and enhances oxygen-reduction performance in polymer-electrolyte-membrane fuel cells. Adv. Mater. 29, 1604556 (2017)
43. J.D. Yi, R. Xu, Q. Wu, T. Zhang, K.T. Zang, J. Luo, Y.L. Liang, Y.B. Huang, R. Cao, Atomically dispersed iron-nitrogen active sites within porphyrinic triazine-based frameworks for oxygen reduction reaction in both alkaline and acidic media. ACS Energy Lett. 3, 883–889 (2018)
44. Y.Z. Su, Z.Q. Yao, F. Zhang, H. Wang, Z. Mics, E. Canovas, M. Bonn, X.D. Zhuang, X.L. Feng, Sulfur-enriched conjugated polymer nanosheet derived sulfur and nitrogen co-doped porous carbon nanosheets as electrocatalysts for oxygen reduction reaction and zinc-air battery. Adv. Func. Mater. 26, 5893–5902 (2016)

45. S.K. Singh, K. Takeyasu, J. Nakamura, Active sites and mechanism of mechanism of oxygen reduction reaction electrocatalysis on nitrogen-doped carbon materials. Adv. Mater. 31, 1804297 (2019)
46. S. Jin, C. Li, L.K. Shrestha, Y. Yamauchi, K. Ariga, J.P. Hill, Simple fabrication of titanium dioxide/N-doped carbon hybrid material as non-precious metal electrocatalyst for the oxygen reduction reaction. ACS Appl. Mater. Interfaces. 9, 18782–18789 (2017)

Publisher's Note